

# Performance of the MICE diagnostic systems

5

A.N. Other et al.

This paper will describe:

- The detectors as we have it installed in the MICE Hall at November 2017
- The performances of the detectors
- The absorbers models and their validation
- The track matching

10

We'll make reference to the published papers wherever possible.

We're targeting the JINST volume.

## 1 Introduction

To include:

15

- Motivation
- Outline of the experiment

## 2 Time-of-Flight Detectors

### 2.1 Introduction

Three time-of-flight detectors (TOF0, TOF1, TOF2) have been built and installed at RAL in 2008 and 2009  
20 to measure the position and the time of crossing particles. TOF0 and TOF1 [1], [2], [3] are placed upstream of the cooling channel, and TOF2 [4] is downstream of the channel, mounted in front of the KL, as shown in Fig. ???. The time of flight between two TOF stations provides particle identification information and can also be used for momentum measurement. TOF1 served most of the time also as an experimental trigger. They have smoothly operated during the so-called Step I and Step IV [5], [6] running periods of the MICE experiment  
25 and were essential for all the measurements done.

The good performances of the TOF detectors, over an extended period of time, has enabled the MICE experiment to characterize fully its muon beams during Step I data-taking, by measuring their emittance [7] and assessing their pion contamination [8].

Each TOF station is made of two planes of fast 1" thick scintillator counters along X/Y directions (to increase  
30 measurement redundancy) read out at both edges by R4998 Hamamatsu fast photomultiplier tubes<sup>1</sup>. R4998 PMTs have been delivered by Hamamatsu in assemblies (H6533MOD) that include the PMT tube, the voltage divider chain and a 1 mm thick  $\mu$ -metal shield, extending 30 mm beyond the photocathode surface. The increase the count rate stability active dividers were used, instead of conventional resistive ones. A simple design with flat fish-tail PMMA light guides, as respect to tilted ones (to reduce the influence of magnetic  
35 field) or Winston cones, has been chosen to optimize the timing detector resolution (favouring the collection of straight light) and to allow an easy mechanical assembly. TOF0, TOF1, and TOF2 have active areas of 40×40 cm<sup>2</sup>, 42×42 cm<sup>2</sup>, and 60×60 cm<sup>2</sup> respectively. The slabs in TOF0 are 4 cm wide, while the slabs of TOF1 and TOF2 are 6 cm wide respectively. The PMTs signal, after ~34 m long RG213 cable and a

<sup>1</sup>one-inch linear focused PMTs with 10 stages, typical gain G~5.7×10<sup>6</sup> at -2250 V and B=0 T, rise time 0.7 ns, transit time spread (TTS) ~160 ps

50% – 50% passive splitter, arrive to a leading-edge CAMAC Lecroy 4115 discriminator followed by a CAEN  
40 V1290 TDC for time measurements and to a CAEN V1724 FADC for pulse-height measurements, to correct time-walk. As reported in reference [2], RG213 cables<sup>2</sup> have a better temperature stability than conventional RG58 cables. Their delay have been individually measured in laboratory, before installation in the experimental hall. Time calibration of individual counters has been done with impinging beam particles by using the detector X/Y redundancy [9].

45 Due to the low residual magnetic field produced by the last quadrupole of the beam line in the proximity of the TOF0 detector ( $\leq 50$  G), the used conventional PMTs had to use elongated  $\mu$ -metal shielding. The other two TOF stations (TOF1/TOF2) had to work instead in the stray fields of the cooling channel solenoids, that are only partially shielded by a 100 mm thick annular iron plates. As residual magnetic fields are up to 0.13 T (with a component along the PMTs axis up to 0.04 T), a local or global magnetic shielding for TOF1 and  
50 TOF2 detectors had to be envisaged. The local shielding option was chosen, at the end, for convenience and easiness of implementation. As magnetic shielding is a mass effect, box-shaped soft iron shielding are more effective than cylindrical ones. This idea pioneered in the D0 experiment has been tested in the case of MICE using different geometrical configuration for the iron shielding boxes and different iron materials (e.g. Fe360, ARMCO<sup>3</sup>, etc). The problem is usually the longitudinal component of the magnetic field, while the orthogonal  
55 component may be more easily shielded. Systematic studies have been done, using a built on purpose solenoid of 23 cm inner diameter, 40 cm length<sup>4</sup> and are fully reported in reference [10]. A composite structure based on the 1 mm  $\mu$ -metal shielding of the H6533Mod assemblies and an external additional  $6 \times 6 \text{ cm}^2$  ( $5.6 \times 5.6 \text{ cm}^2$ ) ARMCO box, 15 cm long, with an internal hole of 3.2 cm diameter has been adopted for the PMT's magnetic shielding of TOF2 (TOF1) [11]. Fig. 1 show how the local shielding has been implemented in TOF2, using  
60 different sheets of ARMCO to make a “single bar structure” for all the PMTs of one side, instead of single boxes for individual PMTs. The effective shielding amounts to  $\sim 6.6$  cm of ARMCO thickness, with extra shielding effect due to the fact that all bars shielding the TOF2 PMTs are magnetically linked between them and to both the KL shielding and the shielding plate making a single magnetic loop. Fig. 2 shows some steps of the assembly procedure for the TOF2 detector at INFN MIB mechanics workshop.

65 For what attains performances, TOF0, TOF1, and TOF2 had timing resolutions around 50-60 ps respectively, over the 8 years running period, consistent with design requirements, with the spatial resolution around 1 cm. Fig. 3 shows distributions of the time of flight between TOF0 and TOF1 where electrons, muons and pions fall into three well defined peaks.

## 2.2 Performance

# 70 3 Cherenkov Detectors

### 3.1 Introduction

The Cherenkov detectors are primarily designed to provide  $\pi$ - $\mu$  separation in the higher momentum ranges, where TOF separation is not sufficient for conclusive particle identification.

In order to provide separation over a large range of momenta, two high density silica aerogel Cherenkov  
75 detectors (CkovA and CkovB) with refractive indices  $n=1.07$  and  $n=1.12$  are used. They are each read out by four 200 mm photomultiplier tubes and placed directly one after another in the beamline, located just after the first TOF counter. In Fig. 4 an exploded view of one detector is shown.

<sup>2</sup>CERN type C-50-6-1, with rated delay 4.08 ns/m

<sup>3</sup>ARMCO steel from AkSteel is a pure iron with a maximal carbon content of 0.025% and very high magnetic saturation

<sup>4</sup>built by TBM srl, Ubondo (VA), Italy

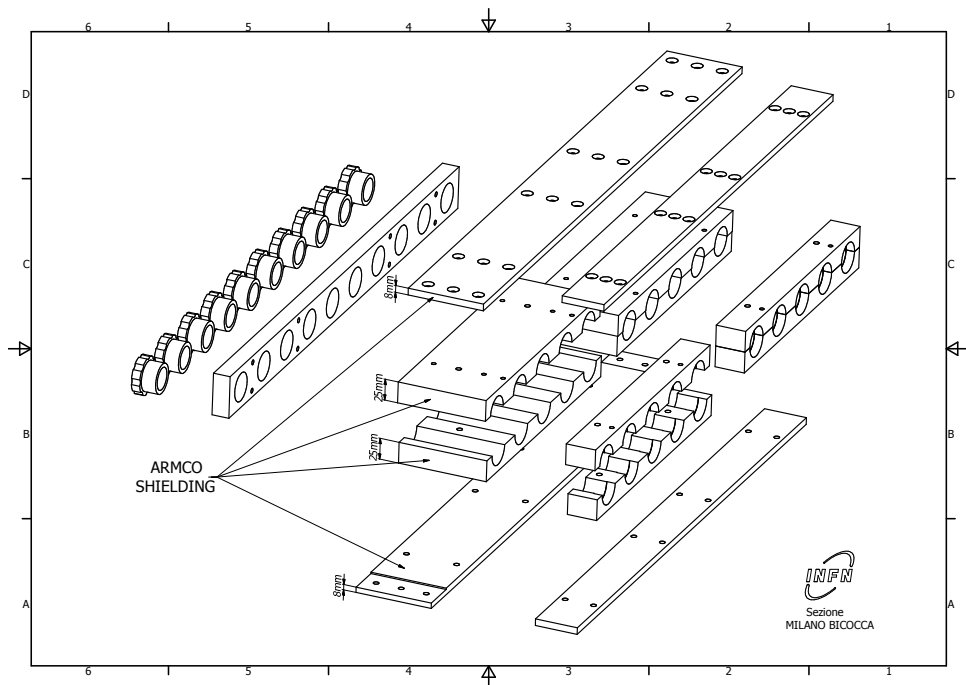


Figure 1: Exploded view of the TOF2 detector magnetic shielding for one row of PMTs.



Figure 2: Assembly of TOF2 at INFN MIB mechanics workshop. Left to right: from the bare magnetic shielding to the installed counters of a plane.

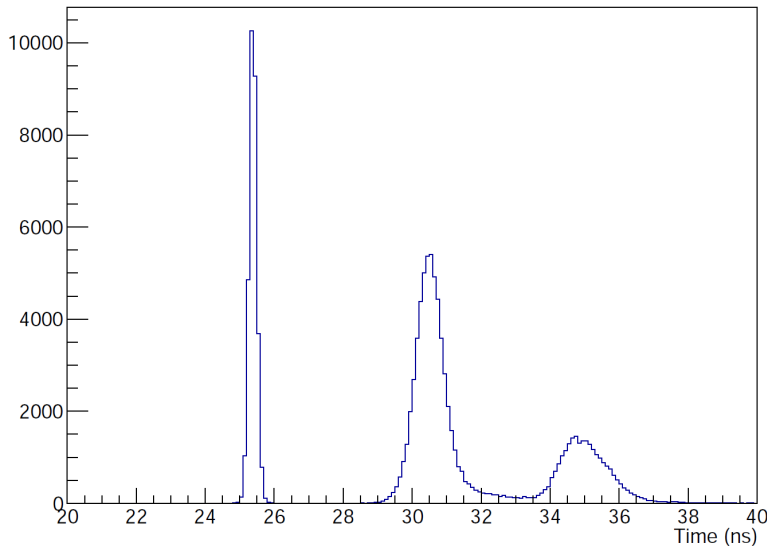


Figure 3: Time of flight between TOF0 and TOF1 for a “pion” beam. From the left: the well separated electron, muon and pion peaks.

Their respective thresholds provide different responses in four distinct momentum ranges, i.e. in the 200 MeV/c beams, pions are below the threshold which would fire the detector for both CkovA and CkovB whereas muons are above only for CkovB, while for the 240 MeV/c beams, pions are above the threshold for CkovB while muons are above for both CkovA and CkovB. Using this information algorithms can be written that produce likelihood distributions of particle type. Below the CkovB muon threshold of about 217.9 MeV/c, where there is no separation, the TOFs provide good separation, whereas the momentum range above the CkovA pion threshold (367.9) MeV/c is outside of the MICE running parameters [12].

### 85 3.2 Performance

## 4 KLOE-Light Calorimeter

### 4.1 Introduction

The KLOE-Light (KL) pre-shower sampling calorimeter is composed of extruded lead foils in which scintillating fibres are placed in volume ratio scintillator:lead  $\sim 2:1$ , “lighter” than the one of the KLOE experiment calorimeter (1:1).

The fibres are 1 mm diameter BICRON BCF-12, scintillating in the blue, 1.35 mm distant from each other within a layer. The distance between two layers is 0.98 mm, one layer being shifted by half the fibre pitch with respect to the next. Scintillation light is guided from each slab into a total of six PMTs (three on each side). Iron shields are fitted to each photomultiplier to mitigate against large stray magnetic fields from the cooling channel (see Fig. 5). The signal from each PMT is sent to a shaping amplifier (SA) module, which shapes and stretches the signal in time in order to match the sampling rate of the flash ADCs (Fig. 6 shows the design of a single slab). A total of 7 slabs forms the whole detector, which has an active volume of  $93\text{ cm} \times 93\text{ cm} \times 4\text{ cm}$ .

With its 2.5 radiation lengths the KL is used to distinguish muons from decay electrons providing energy deposition and timing information and to act as pre-shower in front of the EMR. The detector has been used to estimate the level of pion contamination within the MICE muon beams to be around 1% [8].

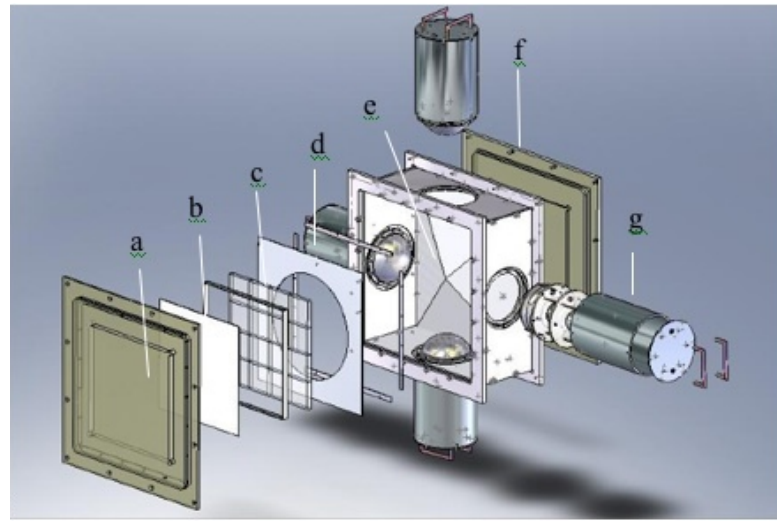


Figure 4: MICE aerogel Cherenkov counter blowup: a) entrance window, b) mirror, c) aerogel mosaic, d) acetate window, e) GORE reflector panel, f) exit window and g) 8 inch PMT in iron shield.

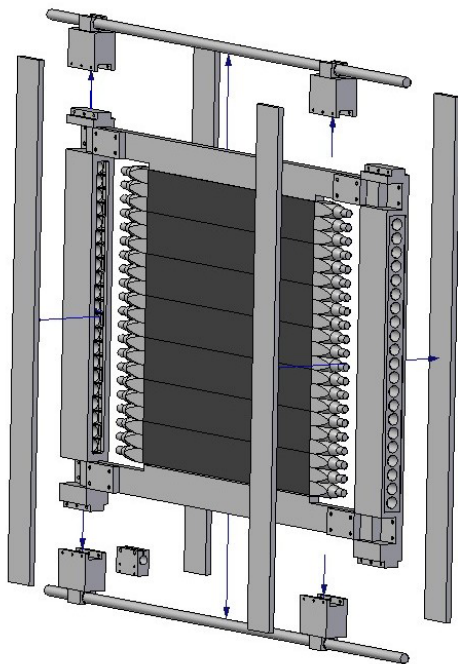


Figure 5: Magnetic shielding of KLOE-Light PMTs.

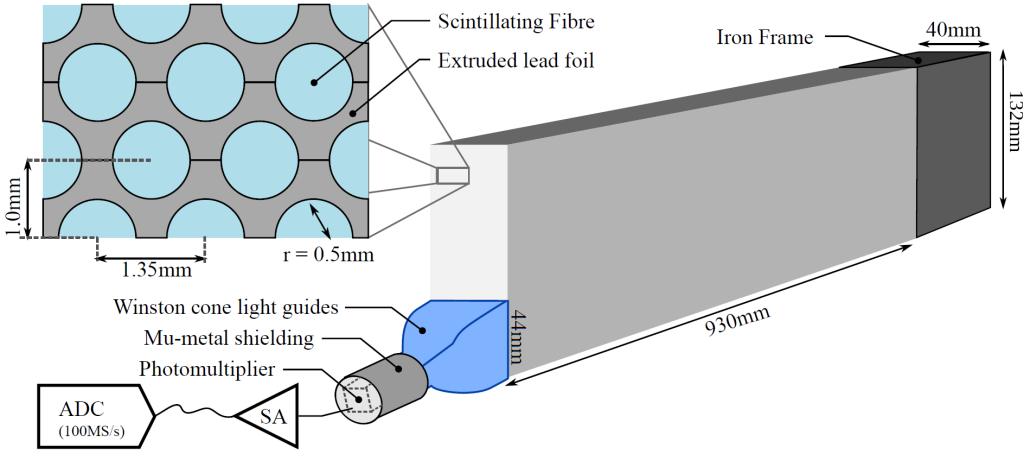


Figure 6: Single slab design of MICE KLOE-Light Calorimeter.

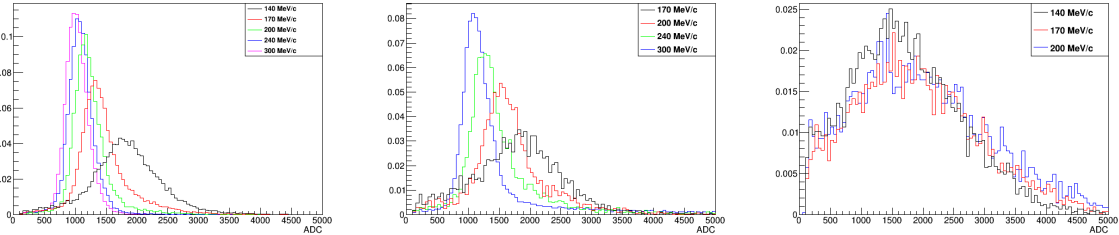


Figure 7: KL response to muons (left), pions (centre) and electrons (right) for several momenta. It is shown charge deposited by particles in KL in arbitrary units. All histograms are normalized to unity.

## 4.2 Performance

The study of KL response to different particle types at different momenta is based on particle identification obtained by time-of-flight detector, as shown in the example of Fig. 3, by applying proper cuts on the time-of-flight spectrum. The performance is presented for 140, 170, 200, 240 and 300 MeV/c momenta at the absorber position, and depending of species population for muons, pions and electrons. The results presented below are obtained from the straight tracks data (i.e. without magnetic fields in the trackers or focus coil) taken mainly in 2017. The KL response to muons, pions and electrons for all available momenta is presented in Fig. 7. It is clear in the cases of muons and pions that they are below mip momenta since energy deposition decreases with momentum increasing<sup>5</sup>.

For comparison of energy deposition of muon, pions and electrons for fixed momentum Fig. 8 is presented. In the case of 300 MeV/c (Fig. 8, right), where muons and pions have almost the same maximum of distribution, the tail of pions is fatter than muon one. This is due to the fact that pions experience strong interaction as well. This pion behaviour has been used to estimate its contamination in muon sample.

The number of fired KL cells by a single muon, electron or pion is given in Fig. 9 for 240 MeV/c beam. For muons we expect one, in some cases two and almost never more fired cells depending on track inclination.

<sup>5</sup>Actually the energy deposition is defined as the sum of ADC products from all cells in KL above a given threshold. The ADC product on the other hand is the product of left and right side of one slab divided by the sum of left and right side:  $ADC_{prod} = 2 \times ADC_{left} \times ADC_{right} / (ADC_{left} + ADC_{right})$ . The factor 2 is present for normalization. The product of two sides compensates the effect of attenuation.

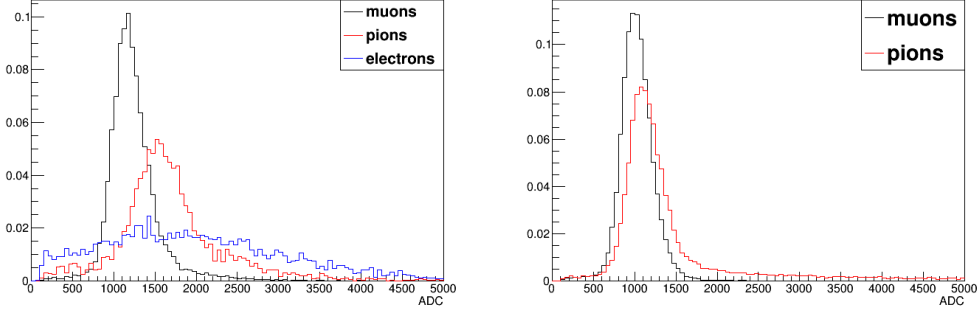


Figure 8: Comparison of energy deposition of muons, pions and electrons at 200 MeV/c (left) and of muons to pions at 300 MeV/c (right).

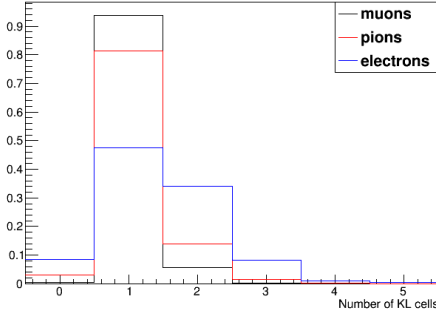


Figure 9: Particle multiplicity for 240 MeV/c, i.e. number of KL cells fired.

Pions and electrons create avalanches in KL and electron ones is much wider than the pion ones as visible of number of KL cell hits. The same figure shows number of events when if there is a reconstructed TOF track, but no signal in KL above the threshold. This can be used to calculate efficiency of KL for the three species as a function of momentum. The results are presented in Table 1 and shows that efficiency for muon registration is close to 99%.

species	<b>140 MeV/c</b>	<b>170 MeV/c</b>	<b>200 MeV/c</b>	<b>240 MeV/c</b>	<b>300 MeV/c</b>
<b>electrons</b>	$0.95 \pm 0.02$	$0.95 \pm 0.01$	$0.94 \pm 0.03$	n/a	n/a
<b>muons</b>	$0.97 \pm 0.02$	$0.99 \pm 0.01$	$0.99 \pm 0.01$	$0.99 \pm 0.01$	$0.99 \pm 0.01$
<b>pions</b>	n/a	$0.89 \pm 0.03$	$0.95 \pm 0.03$	$0.97 \pm 0.03$	$0.98 \pm 0.01$

Table 1: Efficiency of KL for electrons, muons and pions as a function of particle momentum. The conditions required are existing of a TOF track and signal in KL above the threshold. The uncertainties are statistical.

In Fig. 10 is shown simulation of KL response to 300 MeV/c muons and pions and the distributions are compared with data. The agreement between data and simulation is very good. The simulation is done via following steps:

- Smearing of produced photons in scintillator fibres. They obtain Poisson statistic so such is applied. In principle one can replace it with Gaussian because the number of photons created is large enough for such an approximation.

125

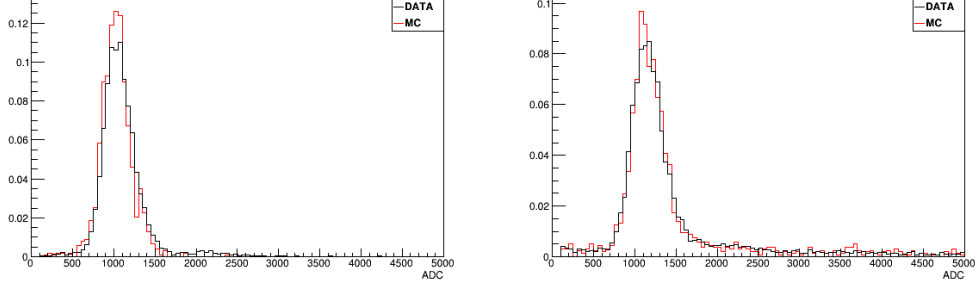


Figure 10: Comparison between data and Monte Carlo simulation of KL response to muons (left) and pions (right) at 300 MeV/c.

- Photoelectrons created on photomultiplier photocathode also have Poisson statistics. It cannot be replaced here with normal distribution because the number of photoelectrons is small enough so such an approximation is illegal.
- Photomultiplier gain obtains also statistical properties but it is neither Poisson nor gauss. Nevertheless it turns out that for simplicity one can use Gaussian distribution with mean value equals to PMT gain and sigma of distribution equals to half of the gain. KL photomultipliers have gain  $\sim 2 \times 10^6$ , so their sigma is simply  $10^6$ .

## 5 Electron Muon Ranger

### 5.1 Introduction

The Electron-Muon Ranger (EMR) is a fully-active scintillator detector [13]. It can be classified as a tracking-calorimeter as its granularity allows for track reconstruction. The EMR consists of extruded triangular scintillator bars arranged in planes. One plane contains 59 bars and covers an area of  $1.27 \text{ m}^2$ . Each even bar is rotated by 180 degrees with respect to the odd one. A cross-section of bars and their arrangement in a plane is shown in Fig. 11. This configuration does not leave dead area in the detector for particles crossing a plane with angles that do not exceed 45 degrees with respect to the beam axis. Each plane is rotated through 90 degrees with respect to the previous one, such that a pair of planes defines a horizontal and vertical ( $x, y$ ) interaction coordinate. The light, produced when a particle crosses a bar, is collected by a wave-length shifting (WLS) fibre glued inside the bar. At both ends, the WLS fibre is coupled to clear fibres that transport the light to a photomultiplier tube (PMT). Signals produced in a plane are read out collectively on one end by a single-anode PMT for an integrated charge measurement and separately on the other by a multi-anode PMTs for individual bar hit reconstruction. The full detector is composed of 24 X-Y modules for a total active volume of  $\sim 1 \text{ m}^3$ .

An array of analyses were conducted to characterize the hardware of the EMR and determine whether the detector performs to specifications [14]. The clear fibres coming from the bars were shown to transmit the desired amount of light, and only four dead channels were identified in the electronics. Two channels had indubitably been mismatched during assembly and the DAQ channel map was subsequently corrected. The level of crosstalk is within acceptable values for the type of multi-anode photomultiplier used with an average of  $0.20 \pm 0.03\%$  probability of occurrence in adjacent channels and a mean amplitude equivalent to  $4.5 \pm 0.1\%$  of the primary signal intensity. The efficiency of the signal acquisition, defined as the probability of recording a signal in a plane when a particle goes through it in beam conditions, reached  $99.73 \pm 0.02\%$ .

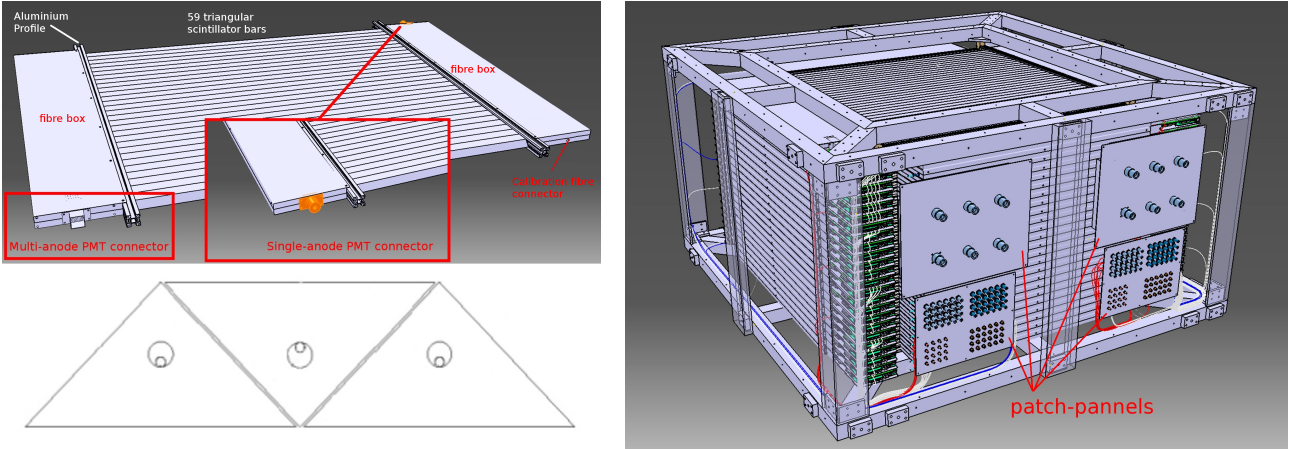


Figure 11: Drawing of one EMR plane (top left), cross section of 3 bars and their wavelength shifting fibres (bottom left) and drawing of the full detector (right).

The primary purpose of the EMR is to distinguish between muons and their decay products, identifying muons that have crossed the entire cooling channel. Muons and electrons exhibit distinct behaviours in the detector. A muon follows a single straight track before either stopping or exiting the scintillating volume, while electrons shower in the lead of the KL and create a broad cascade of secondary particles. Two main geometric variables, the plane density and the shower spread, are used to differentiate them. The detector is capable of identifying electrons with an efficiency of 98.6 %, providing a purity for the MICE beam that exceeds 99.8 %. The EMR also proved to be a powerful tool for the reconstruction of muon momenta in the range 100–280 MeV/c [15].

## 5.2 Performance

An assessment of the latest performance of the detector is produced for the 2017/02 and 2017/03 user cycles.

### 5.2.1 Efficiencies

- Compute the probability of producing a hit in the EMR, getting space points from it;
- Show the global bar/plane multiplicity;
- Show the global charge/plane;
- Show the plane by plane efficiency (MAPMT and SAPMT).

### 5.2.2 Reconstruction

- Show a muon + an electron event (?);
- Show the muon range for different sets of input momentum;
- Show the muon angular distributions + beam profile;
- Show the muon momentum reconstructed, as a function of impinging (?).

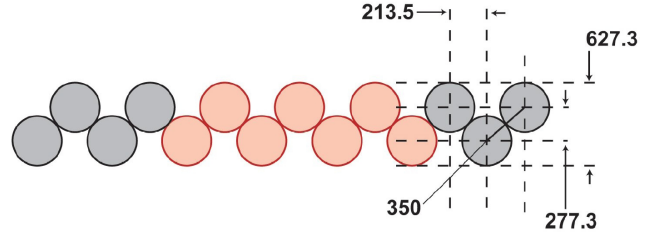
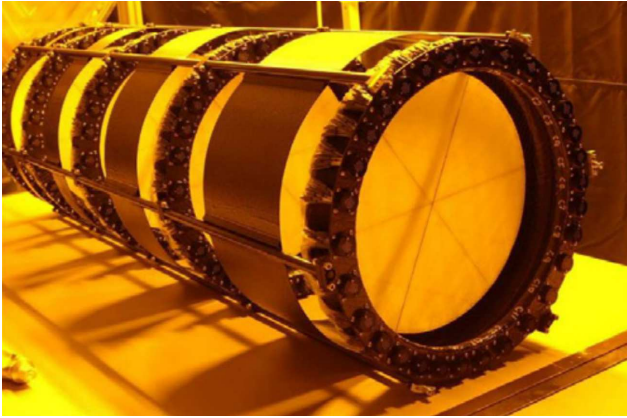


Figure 12: Photograph of one tracker showing the five stations (left) and cross-section of a tracker plane (right)

### 5.2.3 Electron rejection

$$\hat{\chi}^2 = \frac{1}{N-4} \sum_{i=1}^N \frac{\text{res}_{x,i}^2 + \text{res}_{y,i}^2}{\sigma_x^2 + \sigma_y^2} \quad (1)$$

- Show the plane density profiles (e+mu);
- Show the  $\chi^2/\text{ndf}$  (e+mu);
- Compute the contamination;
- Repeat for multiple momenta (200, 240, 170?, 140 futile).

180

## 6 Tracker

### 6.1 Introduction

The emittance measurement in MICE is performed by two scintillating fibre trackers, placed upstream and downstream of the cooling channel, which will allow for the change in emittance across the cooling channel to be measured.

185 The trackers are positioned within the bore of superconducting solenoids used to induce helical motion in the incoming particles, from which position and momentum of the particles can be reconstructed and measured. Each tracker is formed by five stations placed at non-equal intervals to minimize the possible degeneracy in the position measurement Fig. 12 (left). Each station is composed of three planes of doped scintillating fibre of diameter  $350 \mu$ , each orientated at  $120^\circ$ . The fibres are arranged in doublets as in Fig. 12 (right). Scintillation light produced by ionization radiation is readout by visible light photo counters [16].

190 The fibres are grouped into channels (seven fibres per channel). Regarding the tracker reconstruction, hits in individual channel are combined into cluster formed with the neighbour channel. Spacepoints in each plane are then formed from either two or three clusters. Spacepoints are associated with individual tracks using a pattern recognition algorithm before a Kalman filter is applied, accounting scattering and energy loss within the tracker. [17].

## 6.2 Performance

### 6.3 Tracker resolution in field

## 7 PID

### 200 7.1 Introduction

### 7.2 Performance of the PID

## 8 Track Matching

### 8.1 Introduction

### 8.2 Performance

### 205 8.3 Beam based magnet alignment

## 9 Beam-based detector alignment

To carry out its program, MICE requires all of its detectors to reconstruct space points in a globally consistent fashion. A beam-based alignment algorithm was developed to improve the resolution on the position of the scintillating-fibre trackers lodged inside the bores of superconducting magnets. This method can achieve 210 unbiased measurements of the trackers rotation angles with a resolution of  $6 \text{ mrad}/\sqrt{N}$  and of their position with a resolution of  $20 \text{ mm}/\sqrt{N}$ , with  $N$  the number of selected tracks. This section briefly describes the alignment algorithm and presents the results obtained during the 2017/01 ISIS user cycle as an example case. The procedure is described in greater details and cross-checked on several simulations in [18].

### 9.1 Introduction

215 The single-particle nature of the MICE experiment requires reliable global track matching throughout, i.e. the ability to associate a trace measured in the upstream tracker with one in the downstream tracker but also with the particle identification detectors. The many detectors must reconstruct space points in a globally consistent fashion to guarantee reliable and efficient track matching, as well as unbiased muon scattering measurements.

The baseline for the beam-based alignment is the surveys of the detectors in the hall using laser telemetry. 220 Surveys were performed regularly throughout the MICE Step IV commissioning phase and data taking period. The TOF1 time-of-flight hodoscope was moved periodically to access the upstream end of the superconducting solenoids and resurveyed systematically. The downstream particle identification detectors module, composed of TOF2, the KL and the EMR, was also repositioned on occasion. The focus coil module was moved in and out of the beam line to change absorbers. Each of these events was followed by a complete resurvey.

225 The particle identification detectors are each equipped with at least four survey monuments and are surveyed directly. The two scintillating fibre trackers, nested in the superconducting solenoids, can not be accessed. The upstream and downstream flanges of each solenoid are surveyed and the end plate of the trackers are surveyed with respect to the flanges. The estimated position of the trackers within the bores are inferred from these measurements. A laser theodolite is used to locate the monuments with respect to the datum point situated under 230 the second dipole magnet, D2. Figure 13 shows a picture of TOF2 and the location of its survey monuments.

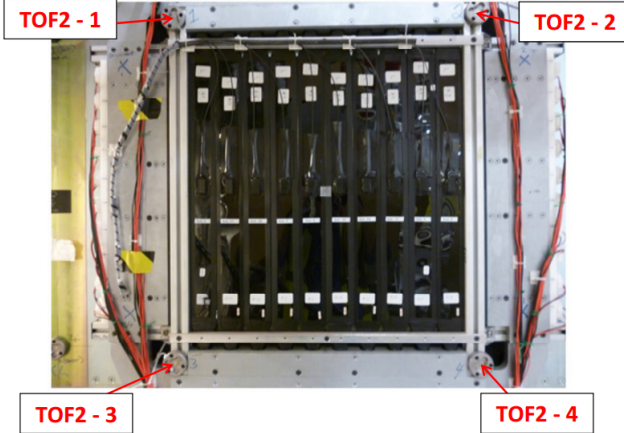


Figure 13: Picture of the TOF2 time-of-flight hodoscope and its four survey monuments labelled TOF2-1–2–4.

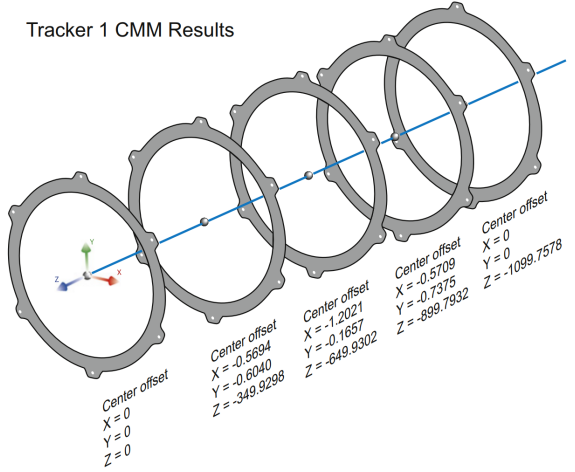


Figure 14: Disposition of the downstream tracker stations along with the CMM measurements of their position with respect to the reference axis.

Before being placed inside the magnets, each tracker was surveyed independently using a coordinate-measuring machine (CMM). This ensures that the position of the five stations is well known within each tracker with respect to the end plate. Figure 14 shows the disposition of the stations in the downstream scintillating fibre tracker and their position as measured by the CMM. The reference position is the axis that joins the centre of station 1 to the centre of station 5. The positions of stations 1 to 3 are measured with respect to that axis. The beam can be used to check the tracker station alignment.

Special care is taken during the installation of the trackers within the magnet bores. The installation platform is adjustable to enable the tracker to be aligned with the bore of the solenoid. The tracker sits on four adjustable feet, two at each end. The adjustable feet are used to align the tracker with the magnetic axis of the solenoid. Once this has been done, the location bracket is fitted. The location bracket locks the tracker in its longitudinal and azimuthal positions.

## 9.2 Analysis method

The position of tracker  $t = u, d$  in global coordinates is entirely defined by the location of its centre  $(x_T, y_T, z_T)$  and a set of Tait-Bryan angles  $(\alpha_T, \beta_T, \gamma_T)$ . The  $z$  axis is oriented along the beam line and points downstream, the  $y$  axis points upwards and the  $x$  axis completes the right-handed coordinate system. The rotation about  $x$ ,  $\alpha_T$ , is called pitch, about  $y$ ,  $\beta_T$ , is called yaw and about  $z$ ,  $\gamma_T$ , is called roll. For a straight track of local coordinates  $(x_t, y_t, z_t)$  at the tracker centre, the global coordinates are reconstructed as

$$\begin{pmatrix} \xi_t \\ v_t \\ \zeta_t \end{pmatrix} = \begin{pmatrix} x_t - \gamma_T y_t + \beta_T z_t + x_T \\ y_t + \gamma_T x_t - \alpha_T z_t + y_T \\ z_t - \beta_T x_t + \alpha_T y_t + z_T \end{pmatrix}. \quad (2)$$

in the first order small angles approximation. The global gradients of the straight track thus read

$$\begin{aligned} \xi'_t &= \frac{d\xi_t}{d\zeta_t} = \frac{dx_t - \gamma_T dy_t + \beta_T dz_t}{dz_t (1 - \beta_T x'_t + \alpha_T y'_t)} \simeq x'_t - \gamma_T y'_t + \beta_T, \\ v'_t &= \frac{dv_t}{d\zeta_t} = \frac{dy_t + \gamma_T dx_t - \alpha_T dz_t}{dz_t (1 - \beta_T x'_t + \alpha_T y'_t)} \simeq y'_t + \gamma_T x'_t - \alpha_T. \end{aligned} \quad (3)$$

There are six potential unknowns per tracker. Some simplifications can be made to lower the amount of unknowns. The  $z_T$  coordinate of each tracker is known to great accuracy from the survey. It may also be shown  
245 that the roll of the trackers has negligible influence on the alignment and may be ignored [18]. The beam-based detector alignment is critical to find the  $(x_T, y_T, \alpha_T, \beta_T)$  constants for each tracker.

The location of the TOFs is used as the reference for the tracker alignment. The line that joins the centre of TOF1 with the centre of TOF2 is chosen to be the reference axis. A deviation from this axis is considered as a misalignment of the trackers. Multiple scattering in the beam line does not allow to do the alignment on single  
250 particle basis but works for a larger sample of particles. The mean residual angles and positions of the trackers with respect to the TOF12 axis are an essential and powerful tool to infer the correction factors.

Each TOF provides a single space point in the global coordinate system  $(\xi_i, v_i, \zeta_i)$  with  $i$  the ID of the TOF. This position is assumed to be the true position with a large uncertainty due to the limited granularity of the detector ( $\sigma_x \sim \sigma_y \sim 17$  mm). The gradients of the track between the two TOFs are reconstructed as:

$$\psi'_{12} = \frac{\psi_2 - \psi_1}{\zeta_2 - \zeta_1}, \quad \psi = \xi, v. \quad (4)$$

The extrapolated position of the TOF reference track in the centre of tracker  $t = u, d$  is

$$\psi^t_{12} = \psi_1 + \frac{\psi_2 - \psi_1}{\zeta_2 - \zeta_1}(\zeta_T - \zeta_1) = (1 - \chi_T)\psi_1 + \chi_T\psi_2, \quad \psi = \xi, v, \quad (5)$$

with  $\chi_T = (\zeta_T - \zeta_1)/(\zeta_2 - \zeta_1)$ , the fractional distance from TOF1 to the tracker centre.

Tracker  $t = u, d$  samples the particle track in five different stations  $(x_t^j, y_t^j, z_t^j)$ , with  $j = 1, \dots, 5$ . This allows for the reconstruction of a straight track with gradients  $x'_t$  (resp.  $y'_t$ ) in the  $xz$  (resp.  $yz$ ) projection and its position at the centre,  $(x_t, y_t, 0)$ . No assumption is made on the prior position of the tracker and hence the coordinates and gradients are returned in local coordinates, i.e. assuming a tracker perfectly aligned with the beam axis, whose centre lies at  $z = 0$ .  
255

In global coordinates, on average, the track reconstructed between TOF1 and TOF2 should agree with the track reconstructed in either tracker, i.e. the mean residuals should be zero. Applying this reasoning to the unknown offset and angles yields the following system of four equations with four unknowns [18]:

$$\begin{cases} \langle x'_t - \xi'_{12} \rangle = -\beta_T \\ \langle y'_t - v'_{12} \rangle = \alpha_T \\ \langle x_t - \xi^t_{12} \rangle = -x_T \\ \langle y_t - v^t_{12} \rangle = -y_T \end{cases}. \quad (6)$$

The measurement of four residual distributions per tracker yields the alignment constants.

The method described here assumes that the mean residuals can be measured with great accuracy and, more  
260 importantly, are unbiased. A bias in one of the residual distributions inevitably introduces a bias in the measurement of the corresponding alignment parameter, as they are directly proportional. The main source of bias is the scattering in the material between TOF1 and TOF2. If the beam is not perfectly centred, particles preferentially scrape out on one side of the magnet bore, anisotropically curbing a specific tail of the residual distribution. To nullify this effect, a fiducial cut is applied to the upstream sample. Only particles that are expected to be  
265 contained in the downstream tracker are included in the analysis [18].

### 9.3 Alignment of the data sample

Data is recorded with the superconducting magnetic channel of the experiment turned off, i.e. with tracks going in a straight line from TOF1 to the beam dump. High momentum beams are used in order to reduce the RMS

scattering angle and maximize transmission. The settings used correspond to ‘pion’ beams of positive polarity  
270 to maximize statistics. The beams exhibit a variety of distributions in the beam line. An agreement between the independent fits guarantees an unbiased measurement of the alignment constants.

Provided with the unbiased sample produced as described in section 9.2, each track yields a set of global gradients between TOF1 and TOF2,  $\xi'_{12}$  and  $v'_{12}$ , and global extrapolated positions at the tracker centres,  $\xi^t_{12}$  and  $v^t_{12}$ . It also records the position of the track at the centre of the trackers in local coordinates,  $x_t$  and  $y_t$ , and  
275 its local gradients,  $x'_t$  and  $y'_t$ . The residual distributions necessary to measure the left hand side of equations 6 are produced in order to measure the eight alignment parameters. Figure 15 shows the gradient residuals between  $y'_u$  and  $v'_{12}$  for run 9367. The mean residual yields the the pitch of the upstream tracker,  $\alpha_U$ .

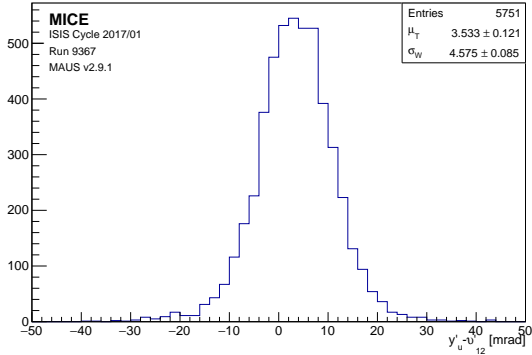


Figure 15: Residuals distribution between the pitch gradients measured locally in TKU,  $y'_u$ , and globally between TOF1 and TOF2,  $v'_{12}$ .

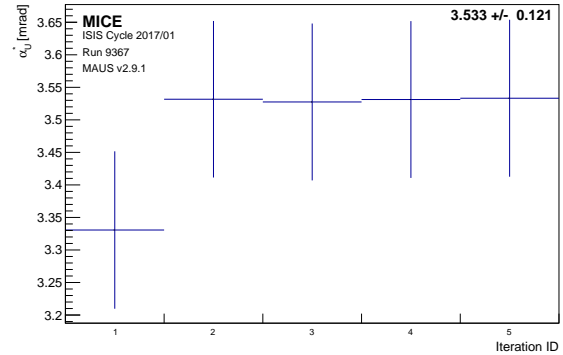


Figure 16: Evolution of the optimal value of the pitch angle in TKU,  $\alpha_U^*$ , for different number of iterations of the fitting algorithm.

To ensure the best possible fit to the tracker parameters, the algorithm is applied multiple times. The first estimate of  $x_T, y_T, \alpha_T, \beta_T$  is used as an input to the sample selection part of the algorithm. The process is  
280 repeated until the alignment constants converge. Figure 16 shows the evolution of the optimal upstream tracker pitch,  $\alpha_U^*$ , over five iterations for run 9367.

Each data set was processed independently with the algorithm. Figure 17 compiles the alignment parameters measured for each run. The measurements are in good agreement with one another and show no significant discrepancy. The constant fit  $\chi^2/\text{ndf}$  is close to unity for each fit, which indicates that there are no significant  
285 additional source of uncertainty. The optimal parameters are summarised in table 2.

	x [mm]	y [mm]	$\alpha$ [mrad]	$\beta$ [mrad]
TKU	$-0.032 \pm 0.094$	$-1.538 \pm 0.095$	$3.382 \pm 0.030$	$0.412 \pm 0.029$
TKD	$-2.958 \pm 0.095$	$2.921 \pm 0.096$	$-0.036 \pm 0.030$	$1.333 \pm 0.030$

Table 2: Summary table of the optimal alignment constants measured in the high-momentum straight-track data acquired during the 2017/01 ISIS user cycle.

## 9.4 Propagation

The fitted parameters are used to yield the global track coordinates at the tracker  $t = u, d$  centres,  $(\xi_t, v_t, \zeta_t)$ , through equation 2 and the global gradients  $\xi'_t, v'_t$  through equation 3. A corrected global track is propagated in an adjacent detector module  $M$  at  $\zeta_m$  through

$$\psi_t^m = \psi_t + \psi'_t(\zeta_m - \zeta_t), \quad \psi = \xi, v. \quad (7)$$

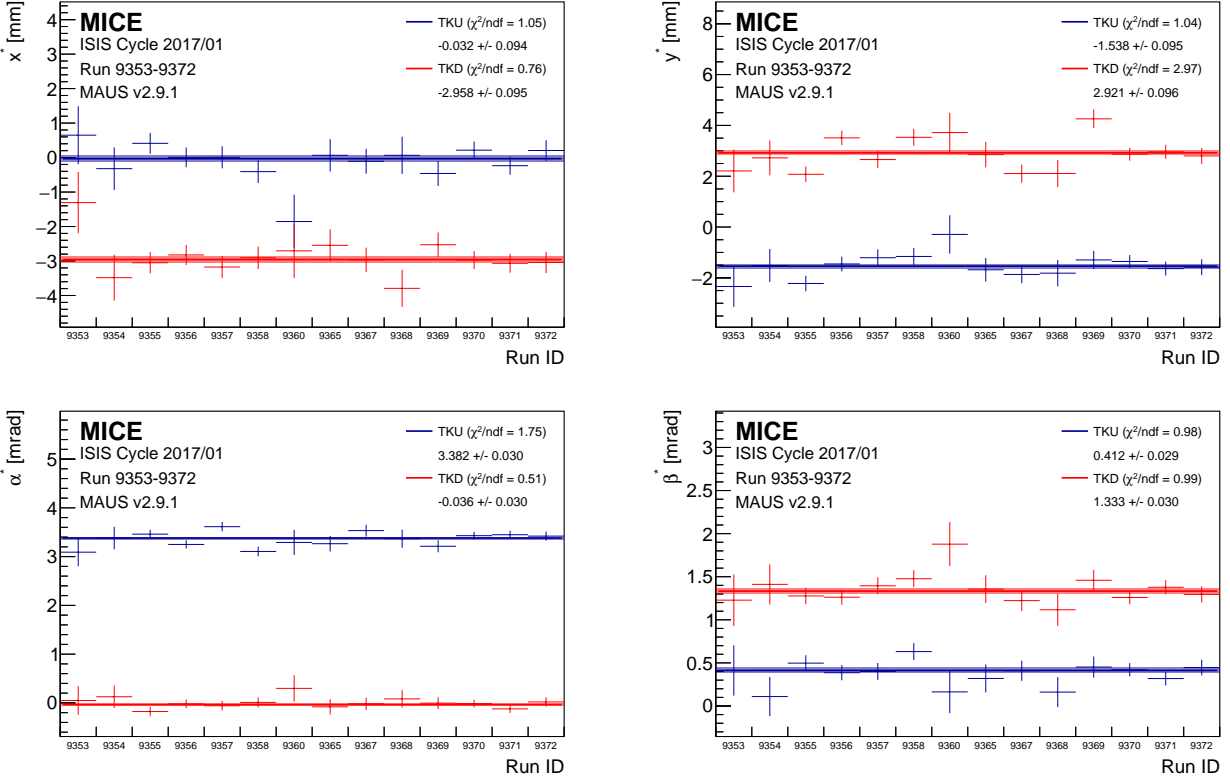


Figure 17: Consistency of the alignment algorithm across runs acquired during the 2017/01 ISIS user cycle.

Provided exact corrections, a detector module  $M$  that measures a global position  $(\xi_m, v_m, \zeta_m)$  verifies

$$\begin{cases} \langle \psi_m - \psi_t^m \rangle = 0 \\ \langle \psi'_m - \psi'_t \rangle = 0 \end{cases}, \quad \psi = \xi, v. \quad (8)$$

As a consistency check, the tracks are first propagated between the two trackers. The results are shown in figure 18. The top left and right distributions show the residuals between the TKU and TKD tracks at the centre of the downstream tracker and at the level of the absorber, respectively. The bottom two histograms show the agreement between the angles measured upstream and downstream. The azimuthal angle residuals show consistency between the roll of the two trackers.

The upstream tracker tracks are extrapolated into TOF1 and the downstream tracker tracks are propagated into the three downstream particle identification detectors: TOF2, the KL and the EMR. The residual plots are represented in figure 19. The values obtained show good agreement between the tracks and the space points measured in other MICE detectors.

Special care is taken when evaluating the central value of the residual distributions. The two trackers and the Electron-Muon Ranger have a sufficient spacial resolution to follow a near-Gaussian distribution. The residuals involving these detectors are fitted with a standard multivariate normal of mean  $\mu$  and width  $\sigma$  between the two half-maximum, i.e. in the range  $\mu \pm 1.1775 \sigma$ . The TOF hodoscopes and the KL do not have a sufficient resolution to produce residuals that follow a Gaussian distribution. A probability density function of the form

$$h(x) = \frac{1}{4W} \left( \tanh \left[ \frac{x - \mu + W}{\sigma} \right] - \tanh \left[ \frac{x - \mu - W}{\sigma} \right] \right) \quad (9)$$

is used in each projection to fit the residuals involving the low granularity detectors. The constant  $\mu$  represents the central value of the residual distribution,  $\sigma$  the residual width and  $W$  the half-width of one of the low-

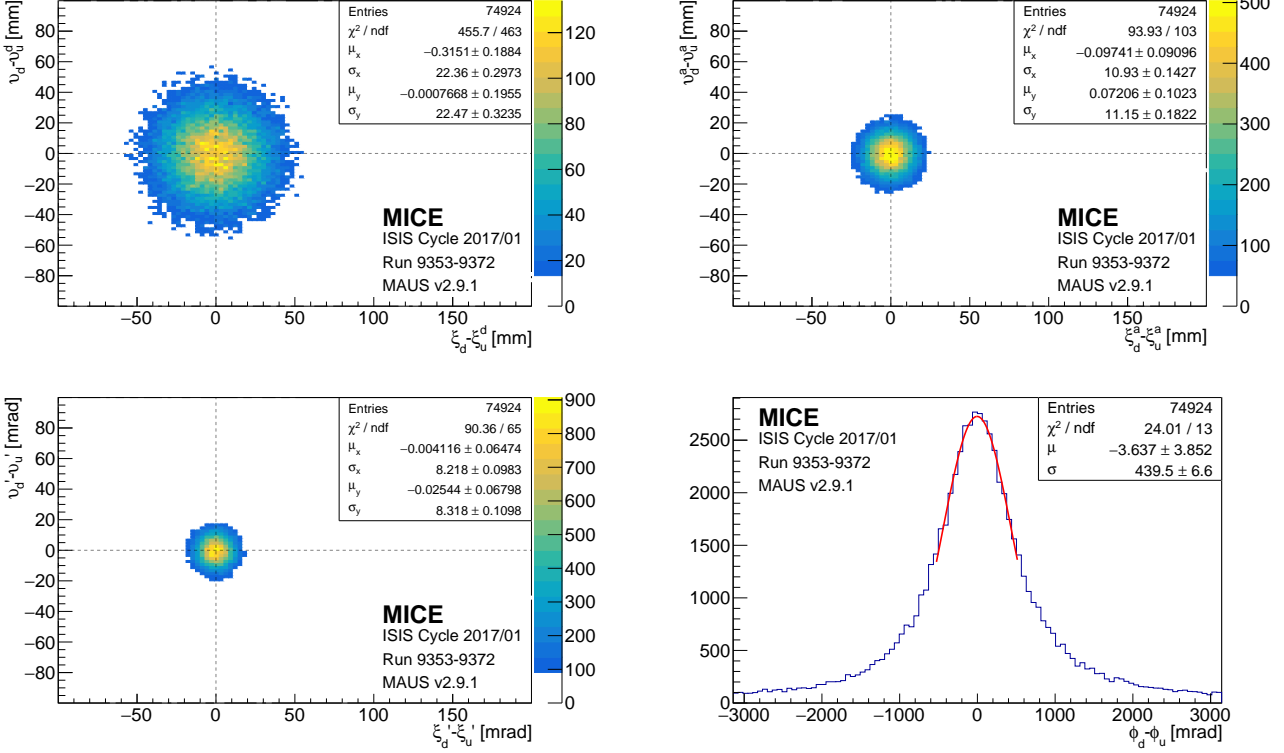


Figure 18: Tracker-to-tracker residual distributions in position (**top**) and angle (**bottom**).

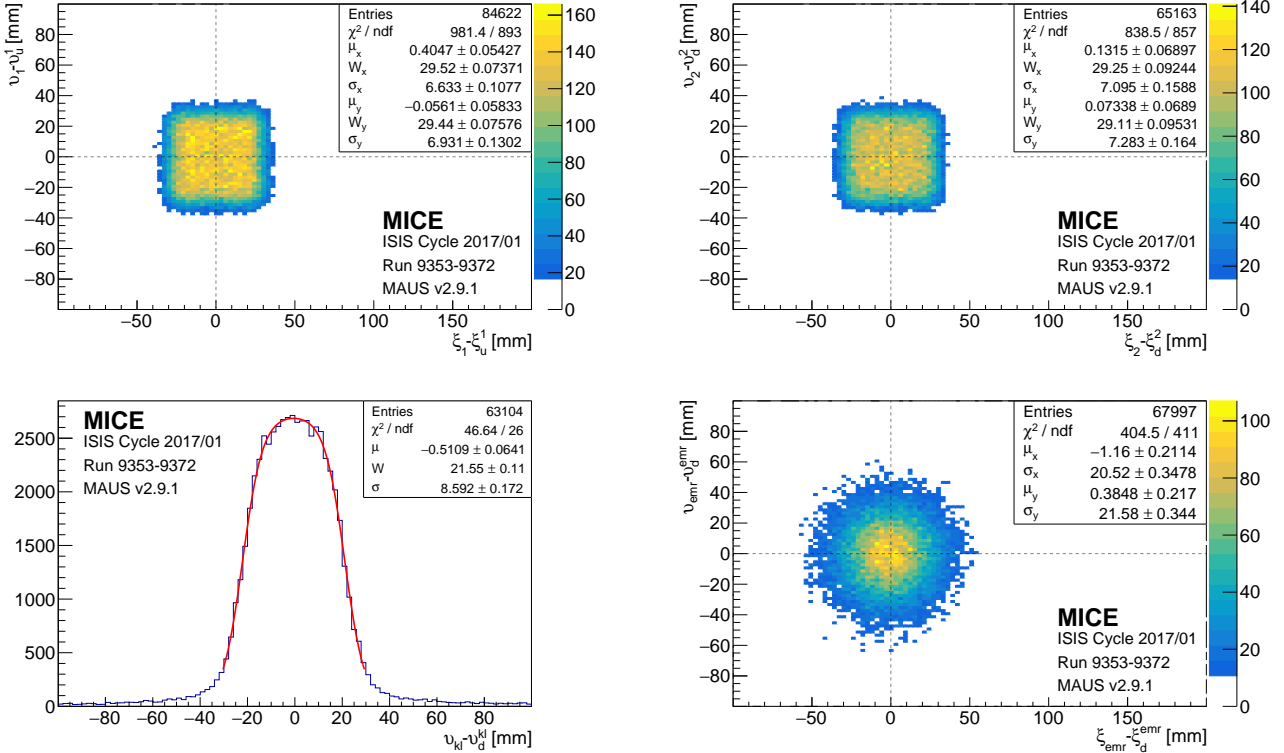


Figure 19: Tracker to particle identification detectors residual distributions (TOF1, TOF2, KL and EMR).

resolution detector pixel. The parameters obtained for each of the fits are represented on the residual graphs. The values found for  $W$  are consistent with pixels of 6 cm in TOF1 and TOF2 and of 4.4 cm in the KL.

300 **10 Magnets and Beam Optics**

**10.1 Introduction**

**10.2 Beam based magnet alignment**

**10.3 Beam line optics**

**11 Absorber**

305 **11.1 Introduction**

**11.2 Validation of the absorber model**

**12 Conclusions**

To be written at last.

## References

- [1] M. Bonesini, “The design of MICE TOF0 detector,” *MICE Note 145* (2006) .  
<http://mice.iit.edu/micenotes/public/pdf/MICE0145/MICE0145.pdf>.
- [2] R. Bertoni *et al.*, “The construction and laboratory tests for MICE TOF0/1 detectors,” *MICE Note 241* (2008) . <http://mice.iit.edu/micenotes/public/pdf/MICE0241/MICE0241.pdf>.
- [3] R. Bertoni, A. Blondel, M. Bonesini, G. Cecchet, A. de Bari, J. S. Graulich, Y. Karadzhov, M. Rayner,  
I. Rusinov, R. Tsenev, S. Terzo, and V. Verguilov, “The design and commissioning of the MICE  
upstream time-of-flight system,” *Nuclear Instruments and Methods in Physics Research A* **615** (Mar.,  
2010) 14–26, arXiv:1001.4426 [physics.ins-det].
- [4] R. Bertoni *et al.*, “The construction of the MICE TOF2 detector,” *MICE Note 286* (2010) .  
<http://mice.iit.edu/micenotes/public/pdf/MICE0286/MICE0286.pdf>.
- [5] D. Rajaram and V. C. Palladino, “The Status of MICE Step IV,”.  
<http://accelconf.web.cern.ch/AccelConf/IPAC2015/papers/thpf122.pdf>.
- [6] M. Bonesini, “Progress of the MICE experiment,” arXiv:1510.08825 [physics.acc-ph].
- [7] The MICE Collaboration, “Characterisation of the muon beams for the Muon Ionisation Cooling  
Experiment,” *ArXiv e-prints* (June, 2013) , arXiv:1306.1509 [physics.acc-ph].
- [8] D. Adams *et al.*, “Pion contamination in the MICE muon beam,” *Journal of Instrumentation* **11** (Mar.,  
2016) P03001, arXiv:1511.00556 [physics.ins-det].
- [9] Y. Karadzhov *et al.*, “TOF detectors Time Calibration,” *MICE Note 251* (2009) .  
<http://mice.iit.edu/micenotes/public/pdf/MICE0251/MICE0251.pdf>.
- [10] M. Bonesini, R. Bertoni, A. de Bari, and M. Rossella, “Behaviour in magnetic fields of fast conventional  
and fine-mesh photomultipliers,” *Nuclear Instruments and Methods in Physics Research A* **693** (Nov.,  
2012) 130–137, arXiv:1207.4909 [physics.ins-det].
- [11] M. Bonesini *et al.*, “The TOF1 local shielding,” *MICE Note 455* (2015) .  
<http://mice.iit.edu/micenotes/public/pdf/MICE0455/MICE0455.pdf>.
- [12] L. Cremaldi *et al.*, “Progress on Cherenkov Reconstruction in MICE,” *MICE Note 473* (2015) .  
<http://mice.iit.edu/micenotes/public/pdf/MICE0473/MICE0473.pdf>.
- [13] R. Asfandiyarov *et al.*, “The design and construction of the MICE Electron-Muon Ranger,” *Journal of  
Instrumentation* **11** (Oct., 2016) T10007, arXiv:1607.04955 [physics.ins-det].
- [14] F. Drielsma, “Electron-Muon Ranger: hardware characterization,” Master’s thesis, University of Geneva,  
2014. <https://arxiv.org/abs/1710.06946>.
- [15] D. Adams *et al.*, “Electron-muon ranger: performance in the MICE muon beam,” *Journal of  
Instrumentation* **10** (Dec., 2015) P12012, arXiv:1510.08306 [physics.ins-det].
- [16] M. Ellis *et al.*, “The design, construction and performance of the mice scintillating fibre trackers,”  
*Nuclear Instruments and Methods in Physics Research Section A: Accelerators, Spectrometers,  
Detectors and Associated Equipment* **659** no. 1, (2011) 136 – 153.  
<http://www.sciencedirect.com/science/article/pii/S0168900211008126>.

- [17] A. Dobbs *et al.*, “The Reconstruction Software for the MICE Scintillating Fibre Trackers,” *MICE Note* 451 (2014) .  
350 <http://mice.iit.edu/micenotes/public/pdf/MICE0451/MICE0451.pdf>.
- [18] F. Drielsma, “Beam-based detector alignment in the MICE muon beam line,” arXiv:1805.06623  
[physics.ins-det]. <https://arxiv.org/abs/1805.06623>.